ASME Journal of Electrochemical Energy Conversion and Storage
Online journal at:
https://asmedigitalcollection.asme.org/electrochemical

Irene Giusti[1]
Department of Industrial Engineering,
Alma Mater Studiorum—University of Bologna,
Bologna 40136, Italy
e-mail: irene.giusti4@unibo.it

Marella De Santis
Department of Industrial Engineering,
Alma Mater Studiorum—University of Bologna,
Bologna 40136, Italy
e-mail: marella.desantis2@unibo.it

Federico Poli
Coesia Engineering Center,
Bologna 40133, Italy
e-mail: federico.poli@coesia.com

Luca Piancastelli
Department of Industrial Engineering,
Alma Mater Studiorum—University of Bologna,
Bologna 40100, Italy
e-mail: luca.piancastelli@unibo.it

Alfredo Liverani
Department of Industrial Engineering,
Alma Mater Studiorum—University of Bologna,
Bologna 40136, Italy
e-mail: alfredo.liverani@unibo.it

Electrode Architecture Effects on Lithium-Ion Battery Aging: A Pseudo-Two-Dimensional Modeling Approach

This study investigates the electrochemical performance and aging behavior of lithium-ion batteries (LIBs), focusing on the architectural effects of electrode and separator geometries alongside active material particle sizes. A pseudo-two-dimensional (P2D) model is employed to simulate lithium intercalation, solid diffusion, and coupled thermal behavior across a full-factorial design space. Despite its one-dimensional formulation, the model provides an optimal balance between computational efficiency and comparative predictive capability. A range of cell configurations is analyzed by varying anode, cathode, and separator thicknesses, as well as particle sizes, to assess their coupled impact on cell performance. The results demonstrate that while smaller particle diameters mitigate solid-state diffusion limitations and enhance capacity retention specifically under high C-rates, minimizing separator thickness significantly reduces inactive mass fractions, boosting baseline specific capacity even in designs with larger commercial particles. However, higher electrode loadings lead to increased volumetric heat-generation rates, particularly within thicker electrode configurations. A comparative assessment is also conducted in terms of cell mass, enabling the estimation of specific energy and power scaled to a standard format. Although limited to relative heat-generation trends by the one-dimensional thermal approximation, the results provide practical guidelines for advanced LIB design, successfully balancing electrochemical performance, volumetric engineering, and computational cost. [DOI: 10.1115/1.4072410]

Keywords: batteries, electrochemical engineering, thermal management

1 Introduction

Lithium-ion batteries (LIBs) are widely valued for their high-energy density and operational efficiency. However, their performance is inherently limited by factors such as phase transitions, instability of the solid electrolyte interphase (SEI), and degradation mechanisms that occur during charge–discharge cycling [1]. Similar to other energy storage technologies, LIBs experience capacity fade and increased internal resistance over time, both during active operation and idle storage. The degradation pathways, distinct for each electrode, are driven by chemical, thermal, and mechanical stressors, all of which are strongly influenced by the electrode material composition. A comprehensive understanding of the aging mechanisms underlying these degradations is essential to address critical issues related to battery lifespan, safety, and performance, as well as to enable reliable lifetime prediction models.

Identifying and characterizing aging mechanisms is inherently complex due to the interplay of multiple factors, including environmental conditions and charging/discharging protocols, which induce different degradation effects. Battery aging is typically categorized into two primary forms: cycle aging and calendar aging. Calendar aging refers to performance decline during storage over time, whereas cycle aging results from repeated charge–discharge operations. The cycle life of a battery is influenced by several operational parameters, including temperature, state of charge (SOC), SOC fluctuations (ΔSOC), charge/discharge rates, cutoff voltages, and charging methodologies [2].

This study explores the electrochemical performance and aging behaviors of LIBs with varying electrode thicknesses and particle dimensions. Through numerical simulations, it evaluates key parameters affecting efficiency, capacity retention, and heat generation. The primary objective is to identify optimization strategies aimed at improving energy density and extending cycle life, with a particular focus on solid-state diffusion, particle size distribution, and separator thickness. The investigation also assesses the impact of mass distribution on thermal behavior and long-term stability. By integrating advanced modeling approaches and differential capacity analysis, this research offers insights that can inform the development of more efficient and reliable LIB designs, particularly for electric vehicles and other high-performance energy applications.

Among the core components of LIBs, the anode and cathode are of particular significance, functioning in tandem with the

[1]Corresponding author.

Manuscript received March 30, 2026; final manuscript received July 22, 2026; published online August 13, 2026. Assoc. Editor: Jun Xu.

electrolyte to facilitate energy storage and release during cycling. Recent advancements have focused on the development of novel materials and nanostructured compounds to enhance battery performance. Notably, high-capacity cathode materials such as nickel-rich lithium nickel cobalt manganese (NCM) oxides have demonstrated promise in increasing energy density and power output. Similarly, silicon and silicon-based composites are being investigated as alternative anode materials due to their significantly higher specific capacity compared to conventional graphite. However, these materials face substantial challenges, particularly with regard to degradation caused by large volume changes during cycling, which can result in capacity loss and reduced battery lifespan.

In the context of rising demand for high-power applications, such as electric vehicles, grid storage, and aerospace systems, the development of LIBs with higher energy densities has become increasingly important. The transition to high-capacity battery chemistry has introduced new challenges in maintaining thermal stability, safety, and long-term efficiency. For example, high-voltage cathodes are susceptible to electrolyte decomposition, while high-capacity anode materials such as silicon suffer from poor structural stability over repeated cycles. These challenges have prompted research into mitigation strategies such as nanoscale engineering to reduce structural changes during cycling, as well as the application of protective coatings to minimize material degradation [3].

In this research, it is well established that the selection of active materials plays a pivotal role in determining the overall performance of lithium-ion batteries. Specifically, the analysis confirmed that nickel manganese cobalt (NMC) oxides, widely used as cathode materials, and graphite, the conventional choice for anodes, continue to demonstrate reliable electrochemical behavior. Moreover, the results clearly indicate that particle size exerts a significant influence on both electrochemical performance and energy efficiency. Smaller particle sizes were associated with enhanced reaction kinetics and better capacity retention, underscoring the critical role of morphological optimization in battery design [4].

A fundamental aspect of LIB operation is the formation of the SEI, a spontaneously formed passivation layer that is crucial for long-term stability and interfacial integrity. The formation of the SEI is typically governed by carefully designed formation protocols. While the SEI layer plays a critical role in enabling the use of anode materials that operate below the electrolyte's electrochemical stability window by inhibiting electron transport and allowing ionic conduction, it also introduces additional impedance. This contributes to capacity fade and overall cell aging [5].

The SEI grows progressively during battery cycling, especially under high voltage and elevated SOC conditions, due to the continued reduction of electrolyte components at the electrode interface. This growth leads to increased impedance, which in turn impairs both ion and electron transport, ultimately reducing energy efficiency and cycle life. Moreover, the ongoing formation of the SEI consumes active lithium, further exacerbating capacity loss. Despite its importance, the atomic-scale structure, composition, and formation mechanisms of the SEI remain only partially understood, which hampers the development of effective strategies to mitigate its negative impact on battery performance [6].

1.1 Novelty and Contribution of This Work. Unlike many previous pseudo-two-dimensional (P2D) studies, which generally investigate the influence of individual design variables through isolated parameter sweeps or sensitivity analyses, the present work proposes a unified physics-based framework for the systematic exploration of lithium-ion battery architecture. Rather than evaluating the effect of a single parameter at a time, the proposed methodology simultaneously investigates the coupled influence of three key structural variables, electrode thickness, separator thickness, and active material particle size, on electrochemical performance, thermal response, and aging behavior within a common computational environment.

A second element of novelty lies in the adoption of a full-factorial (2^3) design strategy to define representative boundary configurations of the design space. Instead of performing independent parameter variations, the simultaneous combination of extreme structural conditions enables the identification of nonlinear interactions and design trade-offs that cannot be observed through conventional one-factor-at-a-time analyses. This approach allows the influence of each design choice to be interpreted within the context of the complete cell architecture rather than in isolation. As a result, the proposed methodology captures interaction effects between structural variables that are generally overlooked in conventional P2D parameter studies based on independent sensitivity analyses.

Furthermore, the proposed framework combines electrochemical performance indicators (specific energy and specific power), one-dimensional thermal analysis, and SEI-based degradation modelling within a single P2D simulation workflow. Although electrochemical, thermal, and degradation models have individually been widely reported in the literature, they are commonly employed to analyze specific aspects of battery behavior. In contrast, the present framework integrates these three domains within a unified simulation environment, allowing their coupled influence to be consistently assessed across multiple electrode architectures under identical operating conditions. This provides a broader and more application-oriented perspective than studies focused exclusively on voltage response, capacity evolution, or thermal behavior alone.

Finally, the principal contribution of this work is methodological rather than the development of new electrochemical equations or degradation models. The proposed framework is intended as a computational screening tool capable of rapidly identifying promising electrode architectures and quantifying the trade-offs between energy density, power capability, heat generation, and long-term degradation before extensive experimental campaigns are undertaken. In this way, the methodology bridges detailed physics-based modelling and practical engineering design, providing a systematic approach for preliminary electrode architecture optimization. Accordingly, the novelty of the present work resides in the proposed methodology for systematic design-space exploration and integrated multiphysics comparative analysis, rather than in the formulation of a new electrochemical model.

2 Materials and Methods

In this work, a set of simulations has been performed in COMSOL MULTIPHYSICS 6.3, in which different combinations of layer thicknesses and particle dimensions have been considered (summarized in Table 1). These analyses aim to characterize the cell's life cycle in terms of state of health and heat generation, as will be described in the following sections. Moreover, a series of simulations were conducted on a one-dimensional (1D) model of a lithium-ion cell. The study systematically explored various configurations by altering the thicknesses of the anode, cathode, and separator layers. Additionally, the effects of varying the particle

Table 1 Geometrical and electrochemical characteristics in the eight modeled cells

Cell type	L_{neg} (μm)	L_{sep} (μm)	L_{pos} (μm)	Rp_{neg} (μm)	Rp_{pos} (μm)	V_{pos}/V_{neg}
Cell 1	55	30	40	2.5	0.25	0.727
Cell 2	55	30	40	8	8	0.727
Cell 3	135	12	87.5	2.5	0.25	0.648
Cell 4	135	12	87.5	8	8	0.648
Cell 5	55	12	40	2.5	0.25	0.727
Cell 6	135	30	87.5	2.5	0.25	0.648
Cell 7	55	12	40	8	8	0.727
Cell 8	135	30	87.5	8	8	0.648

diameters within both the anode and cathode materials were investigated. These parametric analyses aimed to assess the impact of structural and morphological changes on the overall electrochemical performance of the cell.

2.1 Model Parameters. In this section, the main parameters investigated through the simulations are described, and the physical model adopted is presented.

Table 1 reports the key structural and electrochemical parameters of eight different battery cells, focusing on electrode thicknesses, L_{neg} and L_{pos}, for the negative and the positive electrodes, respectively, while L_{sep} is the separator thickness. Furthermore, particle sizes are represented by Rp_{pos} and Rp_{neg} for positive and negative electrodes, respectively. V_{pos}/V_{neg} represents the volume ratio between cathode and anode. These parameters significantly influence the electrochemical performance, transport properties, and overall efficiency of the cells.

Cell 1 has been selected as the reference configuration, with a comprehensive summary of its key characteristics provided in Table 1. Notably, the particle radii are significantly smaller compared to those typically found in commercial materials. Consequently, Cell 1 serves as the baseline configuration for the comparative analysis in this study. It is worth noting that while the active material chemistry simulated throughout this work is strictly NMC811/graphite, the geometric layout and layer thicknesses of Cell 1 were selected taking as a structural guideline the 1D model reported in Ref. [7]. All material-specific electrochemical, thermodynamic, and transport parameters have been fully updated to reflect the NMC811 cathode formulation, thereby maintaining geometric consistency with literature guidelines while investigating an advanced high-energy-density chemistry.

The thicknesses chosen for the three different layers in Cell 3 and Cell 4 are the ones used in a 4680 cylindrical cell, which have been evaluated by Ank et al. within the scope of cell teardown, where the cathode, anode, and separator layer thicknesses have been measured as 87.5 μm, 135 μm, and 12 μm, respectively. Regarding particle dimensions, a diameter ranging from 3 μm to 16 μm is reported in the cathode material and up to 35 μm in the anode material [8]. In the Cell 3 case study, it has been selected to consider ideal particle dimensions, the same as the ones of Cell 1 (2.5 μm is the radius of anode particles and 0.25 μm is the radius of cathode particles). On the other hand, the particle dimensions in Cell 4 represent a commercial material, as in Cell 2, in which it is set equal to 8 μm for both anode and cathode layers.

Cell 5 features thin electrodes (as in Cell 1), a thinner separator (12 μm), and small particle sizes (2.5 μm anode, 0.25 μm cathode), representing an idealized high-rate configuration with minimal diffusion limitations. Cell 6 adopts thick electrodes (as in Cell 3), a thick separator (30 μm), and small particle sizes, exploring the effect of increased electrode loading on performance and thermal behavior. Cell 7 combines thin electrodes, a thin separator, and large particle sizes (8 μm for both electrodes), highlighting the impact of particle growth on rate capability and heat generation in a low-thickness format. Finally, Cell 8 pairs thick electrodes, a thick separator, and large particle sizes, representing a commercially relevant high-energy configuration with expected limitations in diffusion and thermal management.

Rather than performing a conventional single-parameter sensitivity analysis or a statistical design of experiments requiring dense sampling of each variable, this study adopts a physics-based scenario exploration of the design space. The eight configurations correspond to the 2^3 combinations of extreme levels of electrode thickness, separator thickness, and particle size. These cases are intended to represent boundary conditions within the design space rather than to support regression or surrogate modeling. This approach enables the identification of coupled effects and limiting trends in electrochemical, thermal, and aging behavior of lithium-ion cells. Such a strategy is commonly adopted in physics-based electrochemical modeling studies, where computational cost and model complexity restrict exhaustive sampling, and where the primary objective is to capture physically meaningful trends rather than to construct statistically dense response surfaces.

The thickness of electrodes and separators plays a crucial role in determining the electrochemical and thermal performance of lithium-ion batteries. As demonstrated by Zhao et al. [9], increasing the electrode thickness enhances the energy density of the cell due to the higher volume fraction of active materials. However, this advantage is counterbalanced by several detrimental effects. Thicker electrodes exhibit higher internal resistance, which leads to increased ohmic heat generation and exacerbated thermal gradients within the cell. This results in nonuniform temperature distributions, especially near the electrode–separator interfaces, promoting uneven aging of active materials and accelerating capacity fading. Furthermore, under high-rate discharge conditions, cells with thick electrodes suffer from more pronounced concentration polarization and longer diffusion paths, leading to underutilization of active materials and premature termination of discharge. Conversely, cells with thinner electrodes display more uniform heat and ion concentration distributions, better thermal stability, and slower capacity degradation. These findings highlight the critical trade-offs involved in electrode design, underscoring the need for optimized thickness configurations to balance energy density, thermal safety, and long-term electrochemical stability [9].

Electrode volume balancing affects lithium transport, charge storage capacity, and mechanical stability during cycling. The cathode-to-anode volume ratio is given by the following equation:

$$\frac{\mathrm{Vol}_{pos}}{V_{olneg}} = \frac{L_{pos}}{L_{neg}} \tag{1}$$

where Vol_{pos} is the positive electrode volume, Vol_{neg} is the negative electrode volume, and L_{pos} and L_{neg} are the positive and negative electrode thicknesses, respectively. In particular, the effect of the volume balancing is related to the effective potential of the electrodes during battery cycling, and it has been widely reported. It is of critical importance the achievement of electrodes volume balance to ensure uniform reaction kinetics, maximize capacity utilization, and enhance overall cell performance [9].

Concerning the last column of Table 1, it must be emphasized that balancing the capacities of the negative and positive electrodes is an adopted methodology to minimize lithium plating while ensuring optimal performance. This process, named "capacity balancing," often involves slightly oversizing the negative electrode to enhance safety and lifespan. Balancing involves a trade-off between safety, achieved through oversizing the negative electrode and maximizing specific energy, which requires equal capacities for both electrodes. Indeed, oversizing increases inactive material mass, reducing energy density and voltage [10].

The molarity of lithium hexafluorophosphate ($LiPF_6$), in a mixture of ethylene carbonate (EC) and ethyl methyl carbonate (EMC), is influenced by both molality and solution density; therefore, increasing salt concentration leads to an increase in both density and molarity. In fact, EC has a high dielectric constant, which improves salt dissociation, while EMC has low viscosity, which enhances ion mobility; in this manner, the balance between EC and EMC determines the electrolyte's solvation dynamics, which impact electrode passivation and long-term stability. Additionally, the electrolyte properties, such as ionic conductivity and electrochemical stability, are influenced by the solvent ratio and $LiPF_6$ concentration, so that the optimal electrolyte composition enhances battery performance by improving ionic transport and electrode stability. The choice of electrolyte molarity is a trade-off between conductivity, electrode stability (to avoid excessive SEI growth), and cycling performance (to prevent excessive degradation over time) [11,12].

The simulated 1D LIB cells consist of an NCM-based cathode, specifically NMC811, and a graphite-based anode. The electrolyte was set as $LiPF_6$ in 3:7 EC:equivalent circuit model (ECM)

(liquid). In each simulation performed for every cell, the initial electrolyte salt concentration has been set equal to 1.2 mol/L.

The separator material is not explicitly included in the simulations, as the layer thickness corresponding to it is considered composed of electrolyte. However, for thermal analysis and post-processing, a polymeric separator with a density of 1300 kg/m^3 has been assumed [7].

The particle size of both anode and cathode materials plays a crucial role in lithium-ion battery performance because it affects electrode density, lithium-ion transport, mechanical stability, and degradation mechanisms. Smaller particles, approximately 5 μm in diameter, feature shorter diffusion pathways, thereby improving rate capability. However, their increased surface area also promotes electrolyte decomposition and side reactions, which can lead to higher interfacial resistance and accelerated capacity degradation. Conversely, larger particles (15–20 μm in diameter) contribute to higher tap density even if their extended lithium-ion diffusion distances can hinder ionic transport, potentially reducing charge/discharge efficiency, particularly at high C-rates. An optimal particle size distribution must therefore strike a balance between electrode density and electrochemical kinetics, ensuring both efficient ion transport and structural stability to maximize battery performance and longevity [12,13].

Cell 1 has been chosen as the reference case, and a detailed overview of the main characteristics selected is reported in Table 1; the particle radii are particularly small with respect to commonly used commercial materials. For this reason, Cell 1 represents the starting point of the cells comparison in the analyses performed, taking as guideline a 1D isothermal simulation of a LMO ($Li_yMn_2O_4$)/graphite cell [7]; instead, Cell 2 differs from Cell 1 for what concerns the particle radii chosen because in this last case they reflect the characteristics of commercial materials, where a radius of 8 μm is a reasonable trade-off [8].

2.2 Simulation Setting. Each simulation has been developed and run in COMSOL MULTIPHYSICS 6.3.

The mesh setting consists of a physics-controlled mesh type in which the element size has been set as *normal* (see Fig. 1), so the total number of nodes is equal to 50 in Cell 1, Cell 2, Cell 5, and Cell 7, and it is equal to 44 in Cell 3, Cell 4, Cell 6, and Cell 8.

The choice of the normal mesh setting was based on a preliminary mesh independence analysis performed using an extremely fine mesh, consisting of approximately 100 nodes, nearly twice the number employed in the normal mesh configuration. The purpose of this analysis was to verify numerical convergence and assess the sensitivity of the simulations to spatial discretization. The corresponding results (reported in Fig. 10), obtained with the finer mesh, were found to be practically identical, with the curves exhibiting almost perfect overlap for all tested cells under different C-rate conditions. Therefore, the normal mesh was deemed sufficient to provide mesh-independent solutions while significantly reducing computational time.

It should be emphasized that this comparison does not constitute an experimental validation of the model. Rather, it demonstrates the numerical convergence of the adopted discretization scheme. The electrochemical and thermal parameters employed in the simulations were adopted from literature sources and established P2D formulations. Consequently, the objective of the present work is not to recalibrate the electrochemical model but to employ a well-established electrochemical–thermal–aging framework for the comparative assessment of different cell architectures under identical operating conditions.

Furthermore, considering the micrometer-scale thicknesses of the battery layers investigated, the spatial resolution associated with the normal mesh remains sufficiently high to capture the relevant electrochemical and transport phenomena. Increasing the number of nodes through a finer mesh does not significantly improve the representation of these processes while substantially increasing computational cost. This mesh selection therefore provides an appropriate balance between numerical accuracy and computational efficiency, which is particularly important for long-term cycling simulations involving multiple cell configurations.

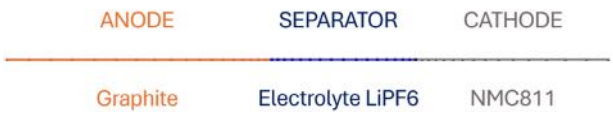

Fig. 1 Schematic representation of the 1D cell model, divided into three segments: the negative electrode (left), the separator (center), and the positive electrode (right). The structure is discretized into a computational "normal" mesh for the simulation.

2.3 Pseudo-Two-Dimensional Computational Model. The mathematical model selected for these analyses is a P2D model, which is better adapted to study a 1D cell configuration than a single particle model (SPM), maintaining manageable computational power requirements. The SPM is a simplification of the P2D model in which the electrodes are assumed as a single spherical particle and the influence of electrolyte concentration gradients is disregarded [14]; however, since electrolyte mass-transport limitations are not considered, the SPM applies exclusively to low C-rate applications (C-rate < 1) [15].

Among the different models developed to simulate lithium-ion cells, there exist two main alternatives: the SPM and the P2D model. In 1996, Doyle and Newman evaluated the predictive capabilities of the P2D model by comparing its results with their experimental data. Subsequent studies have further validated the accuracy of the P2D approach in modeling lithium-ion batteries, and furthermore, in cases where reliable experimental data were unavailable, the predictions generated by the P2D model are reliable and can be utilized as reference benchmarks. Instead, the SPM model has been introduced by Zhang et al. in 2000 as a simplification of the P2D model, which is based on two main hypotheses: (1) the anode and cathode are represented as two spherical particles where the processes of intercalation and deintercalation take place and (2) fluctuations in electrolyte concentration and potential are assumed to be negligible [16].

The pseudo-2D model couples the macro-scale transport phenomena along the cell thickness with the micro-scale solid diffusion within the active material spherical particles. Current collectors are integrated into the framework as boundary conditions at the outer boundaries of the porous electrode domains, establishing the electrical and thermal connection with the external tabs. The term "pseudo" arises because the second dimension pertains to the electrode's radial direction rather than a true second spatial dimension. While the model functions similarly to a one-dimensional framework, it incorporates additional factors such as ion diffusion within the electrolyte and solid electrode phases, as well as Butler–Volmer kinetics for describing electrode reactions. This model is constructed using partial differential equations that link lithium-ion concentration and the potential within both the electrode and electrolyte to the current flow. These variables are analyzed over time along the particle radius and the cell length. Compared to the one-dimensional model, the pseudo-2D model provides enhanced capabilities, including the ability to estimate electrolyte concentration and potential, as well as electrode concentration and potential within the electrode. Additionally, it captures the electrolyte potential and concentration within the separator. However, a limitation of this model is its inability to depict the current density distribution across the electrode surface [17].

Regarding the fundamental equations implemented in the P2D model, the key characteristics are the concentration of solid-state Li^+ ions within the electrodes, which is determined based on Fick's law of diffusion for spherical particles, and the concentration of liquid-phase Li^+ ions in both the electrolyte and separator,

which is formulated according to the principle of Li^+ ion conservation. In addition, the solid-state potential in the electrodes is obtained from Ohm's law, while the liquid-phase potential in the electrolyte and separator is derived using Kirchhoff's and Ohm's laws. The flux of Li^+ ions at the pore walls within the electrodes is characterized by the Butler–Volmer kinetics equation [16].

The reasons explained above justify the selection of the P2D model, in particular because it captures lithium intercalation and deintercalation processes at the electrode surfaces and models the diffusion of lithium ions within solid particles, essential for understanding rate capabilities and concentration gradients. To be concise, it is a better compromise between the computational power required to solve its set of equations and the ability to predict the physics of the problems under study, allowing the introduction of modifications to better predict the behavior of the specific LIB analyzed, as done by Yu et al. [18]. Instead, an analysis of performance degradation in an NMC811/graphite cell through a P2D model has been validated by Both et al. [19], by means of a comparison between experimental data and results coming from simulations.

For each of the eight configuration cases, the charging and discharging profiles were obtained in the CCCV charging and CC discharging modes, setting the voltage range between 2.5 and 4.1 V. Subsequently, the aim was to derive the voltage profiles with respect to capacity during the discharging phase at different C-rate conditions. By means of these profiles, the specific energy and the specific power were calculated. In particular, the specific energy output during discharge was determined by the integral of the discharge voltage over the discharge capacity divided by the total electrode mass, as in the following equation:

$$\bar{E} = \frac{\int V\, dq}{m_{\text{tot}}} \tag{2}$$

Which, in turn, is equal to the area under the cell voltage profile in a cell voltage discharge capacity plot. In lithium-ion cells, the cell voltage depends on the state of charge and is influenced by electrode materials, discharge currents, and operating temperatures. The power output instead was calculated as in the following equation:

$$P = \frac{\bar{E}}{t_d} \tag{3}$$

where t_d was the discharge time. The values of specific energy and power are plotted in a Ragone plot to verify that the battery effectively belongs to the correct region of it.

The Ragone plot serves as a widely recognized method for characterizing energy storage systems by illustrating the nonlinear relationship between the energy extractable from storage and the corresponding discharge power [20]. This energy–power relationship, as depicted in a Ragone plot, can be expressed through either specific values (e.g., energy and power densities) or normalized parameters. The Ragone plot is a valuable analytical tool that warrants broader and more systematic application. It effectively visualizes the energy–power trade-off, reflecting the inherent relationship between available energy and discharge power for a given energy storage system [21].

Considering the different methods used to analyze battery cell aging mechanisms, one possibility is identified in the differential voltage (dV/dQ) curve, which is derived by differentiating the charge/discharge voltage with respect to capacity [22,23].

Furthermore, the thermal analysis has been coupled to the electrochemical one by introducing *Electrochemical Heating* Multiphysics in COMSOL MULTIPHYSICS 6.3 for understanding the heat generation, transfer, and the resulting temperature distribution within LIB during both charging and discharging phases. As will be better explained later, temperature affects reaction rates and lithium diffusion, impacting the battery's performance. The introduction of this investigation shows how different charge and discharge rates influence heat generation and temperature rise, with higher rates causing more significant thermal effects [24].

In particular, the *Heat Transfer in Solids* is considered, where each of the three layers is considered as a solid with its specific properties, such as thermal conductivity, density, and heat capacity at constant pressure, and the heat transfer coefficient has been set equal to 10 ($h = 10$) at the extreme points of the cell's section.

All electrochemical, thermal, and aging boundary conditions applied in the simulations, including current density, voltage limits, heat transfer coefficients, and initial states, are summarized in Table 3 for completeness and clarity.

The *Heat Transfer in Solids (ht)* COMSOL MULTIPHYSICS 6.3 interface serves as a framework for modeling thermal energy transfer within solid materials, encompassing the mechanisms of conduction, convection, and radiation. The temperature equation governing solid domains is derived from the differential formulation of Fourier's law, with potential additional terms accounting for contributions such as heat sources [25].

Starting with the heat balance equations, the *Heat Transfer in Solids* solves the following equation:

$$\rho C_p(\partial T/\partial t + u_{\text{trans}} \cdot \nabla T) + \nabla(q + q_r) = -\alpha T(dS/dt) + Q \tag{4}$$

where ρ is the density (kg/m^3), C_p is the specific heat capacity at constant stress ($J/(kg\,K)$), T is the absolute temperature (K), u_{trans} is the velocity vector of translational motion (m/s), q is the heat flux by conduction (W/m^2), q_r is the heat flux by radiation (W/m^2), α is the coefficient of thermal expansion (K^{-1}), S is the second Piola–Kirchhoff stress tensor (Pa), and Q contains additional heat sources (W/m^3).

In steady-state scenarios, the temperature remains invariant over time, leading to the elimination of terms involving time derivatives. The leading term on the right-hand side of Eq. (4) represents the thermoelastic damping, which characterizes the influence of thermoelastic effects in solid materials:

$$Q_{\text{te}}d = -\alpha T(dS/dt) \tag{5}$$

The second part of the study is focused on the evaluation of the battery state of health (SOH), which has been simulated considering the capacity fading due to the incrementation of the SEI layer and the capacity reduction, which results from the charging and discharging cycles. To fulfill this purpose, a mathematical model, developed by Ramadass et al. [26], has been implemented in such a way as to represent the formation of the SEI layer during the charging/discharging cycles.

In the present model, the growth of the SEI layer is updated at the end of each complete charge/discharge cycle. During the cycle itself, however, the SEI thickness is held constant and does not evolve continuously with time. This approach assumes that the major contribution to SEI formation occurs cumulatively over entire cycles, rather than incrementally at each time-step, thereby simplifying the simulation while still capturing the long-term degradation effects associated with SEI growth.

Table 2 Energy and power of the different cell configurations applied to a 18650 cylindrical cell format

Configuration	Cell 1	Cell 2	Cell 3	Cell 4	Cell 5	Cell 6	Cell 7	Cell 8
Energy (Wh)	13.69	13.47	15.66	16.58	17.61	7.41	17.19	7.25
Power (W)	2.78	2.74	3.22	3.41	3.54	1.51	3.53	1.51

The total film resistance at any charge cycle N is modeled as

$$R_{\text{film}}^{N} = R_{\text{film}}^{N+1} + R_P(t)^N \tag{6}$$

where R_{film}^{N} is the film resistance at the previous cycle, while $R_P(t)^N$ is the resistance due to the newly formed film during the current cycle.

The SEI film thickness growth is given by the following equation:

$$\frac{\partial \delta_{\text{film}}}{\partial t} = \frac{J_s M_P}{a_n \rho_P F} \tag{7}$$

where the side reaction current density J_s is given by Eq. (8), in which η_s is the overpotential, i_{os} is the exchange current density for side reactions, and is the cathodic transfer coefficient of the electrochemical reaction:

$$J_s = -i_{\text{os}} a_n e^{-(a_c n f \eta_s)} \tag{8}$$

$M_P = 7.3 \times 10^4$ mol/kg is the molar mass of the SEI product and $\rho_P = 2.1 \times 10^3$ kg/m^3 is the density of the SEI; in general, they are parameters for the solvent reduction side reaction. Instead, F is Faraday's constant, equal to 96,487 C/mol, and a_n is the negative electrode specific surface area.

At the end of each cycle, the film resistance is updated according to the following equation:

$$R_{\text{film}}^{N} = R_{\text{film}}^{N-1} + \frac{d_{\text{film}}}{k_P} \tag{9}$$

where d_{film} is the film thickness and k_P is the electrical conductivity (in S/m) of the SEI film.

Although lithium-ion battery degradation involves multiple concurrent mechanisms, including lithium plating, active material cracking, and cathode structural degradation, the present model focuses exclusively on SEI growth as the dominant aging mechanism for graphite-based anodes under the investigated cycling conditions. This assumption is justified by the fact that SEI formation is widely recognized as the primary contributor to long-term capacity fade in graphite-based lithium-ion cells, particularly under moderate C-rate operation. The objective of this work is not to reproduce all possible degradation pathways but to capture the dominant trend governing capacity loss and resistance growth within a physics-based reduced-order framework. The model remains modular and can be extended to include additional degradation mechanisms in future studies.

In particular, for each case presented in Table 1, the battery cell has been subjected to 2500 cycles at different C-rates (1C, 2C, 3C, and C/5), and the cooling mechanism at the extreme points of the 1D cell has been modeled through a heat transfer coefficient h equal to 10. This value represents a nonforced cooling of the battery by simply applying an air flux [27].

The objective of this work is to investigate the influence of various parameters, such as electrode thickness and the cathode and anode particle dimensions, on the cell's performance in terms of energetic density and power, and the projection of those variables on state of health, taking into account the thermal aspects that impact the life cycle. These studies aim to identify trends and relative effects of different design choices rather than to propose entirely new physical phenomena. By leveraging the P2D model, which, although simplified, captures the primary trends in lithium-ion transport, temperature evolution, and SEI growth, the methodology allows rapid evaluation of multiple cell configurations. This approach provides a practical and efficient framework for screening electrode and separator designs, offering valuable guidance for experimental and industrial optimization efforts without the need to fabricate and test a large number of physical cells.

The purpose of this work is not to introduce new degradation mechanisms or novel electrochemical equations but to demonstrate how a unified electrochemical–thermal–aging framework can be employed as a computational screening tool for evaluating coupled design trade-offs. In contrast to conventional single-parameter P2D studies, the investigated configurations represent combinations of structural variables, allowing the identification of limiting trends and interactions among particle size, electrode thickness, separator geometry, and heat generation. Therefore, the contribution of the present work lies in the integrated assessment of performance, thermal behavior, and aging within a common physics-based framework intended to support preliminary cell design and experimental planning.

The P2D framework is modular in nature, allowing additional degradation phenomena, such as lithium plating, particle cracking, or other aging effects, to be incorporated through empirical or semiempirical sub-models. Extended P2D models have been used to simulate lithium plating and assess its impact on long-term cell performance [28]. Review studies further demonstrate that combinations of degradation mechanisms, including SEI growth, lithium plating, and particle fracture, can be modeled jointly to capture complex aging pathways [29]. Empirical aging models have also been developed to predict capacity fade and resistance growth under various operational conditions, providing practical ways to extend simplified models for more comprehensive design analyses [30].

2.4 Model Validation. To assess the predictive capability of the adopted electrochemical model, a basic validation was carried out by comparing the simulated discharge voltage profile with experimental measurements acquired on a commercial cylindrical 4680 graphite/NMC811 lithium-ion cell with a nominal capacity of 22 Ah. The experimental dataset was obtained within our research activities and corresponds to the same measurements previously employed for the development and validation of an ECM presented in our earlier work [31]. Although the experimental discharge curve was not explicitly reported in that publication, it constituted the reference dataset used for the identification and assessment of the reduced-order ECM. In the present work, the same experimental measurements are employed for a different purpose, namely to assess the capability of the physics-based P2D model to reproduce the global discharge behavior of a representative commercial graphite/NMC811 cylindrical cell. Once the predictive capability of the electrochemical framework was verified through this comparison, the validated modeling approach was consistently applied to all the cell configurations investigated in the present study.

The validation was performed under the same operating conditions adopted during the experimental tests, namely a constant-current discharge at 1C under ambient temperature conditions. The electrochemical model was simulated using the material properties and electrochemical parameters adopted throughout the present study. The agreement between the simulated and experimental voltage profiles confirmed that the adopted literature-based parameter set provides a sufficiently accurate representation of the reference cell for the intended comparative analyses. Consequently, no additional parameter tuning was introduced for the subsequent simulations, ensuring that all investigated cell configurations were evaluated under the same validated modeling assumptions.

Figure 2 compares the simulated and experimental discharge voltage profiles. A good agreement is observed over the entire discharge process, with a maximum deviation of approximately 2.7% between the simulated and experimental voltage values. The model accurately reproduces the initial voltage plateau, the progressive voltage decrease throughout the intermediate state-of-charge region, and the characteristic voltage drop occurring close to the end of discharge. Minor discrepancies are visible in the intermediate SOC range, where the simulated voltage is slightly higher than the experimental measurement. These differences are reasonably attributed to uncertainties associated with electrochemical material properties, manufacturing tolerances of the commercial cell, and the simplified one-dimensional representation adopted by the

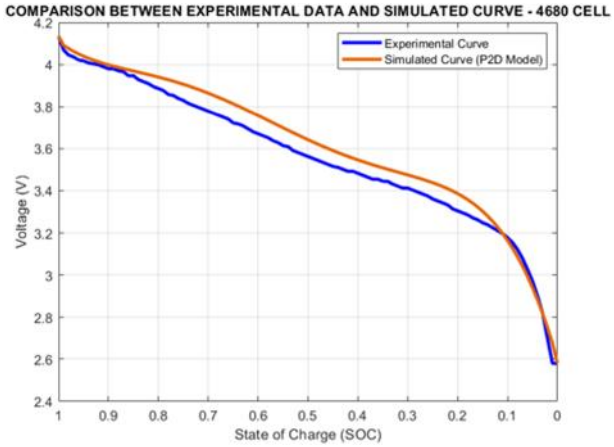

Fig. 2 Comparison between the experimental discharge voltage profile of a commercial 22 Ah 4680 graphite/NMC811 lithium-ion cell and the voltage profile predicted by the adopted P2D electrochemical model during a constant-current discharge at 1C

P2D framework. Nevertheless, the overall agreement, together with the limited maximum deviation, confirms that the model successfully captures the dominant electrochemical behavior governing the discharge process.

The purpose of this validation is not to develop a fully calibrated digital twin of the investigated commercial battery, but rather to demonstrate that the adopted electrochemical framework reliably reproduces the global discharge behavior of a representative 4680 graphite/NMC811 lithium-ion cell. This validation therefore provides the necessary confidence to employ the model as a physics-based computational screening tool for the comparative investigation of the influence of particle size, electrode thickness, separator geometry, thermal behavior, and aging trends discussed in the remainder of this work.

2.5 Model Limitations. Although a basic validation against the experimental 1C constant-current discharge profile of a commercial 22 Ah 4680 graphite/NMC811 lithium-ion cell has been presented in Sec. 2.4, the present work primarily relies on electrochemical, thermal, and aging parameters adopted from the literature to perform the extensive factorial study. Consequently, while the global electrochemical behavior of the reference cell has been verified, the long-term aging mechanisms and coupled thermal simulations across the different configurations should be interpreted primarily in terms of comparative trends rather than absolute quantitative predictions.

Since all cell configurations are analyzed using the same governing equations, material properties, and boundary conditions, the model provides a consistent framework for comparing the influence of electrode thickness, separator geometry, and particle size on electrochemical performance, heat generation, and degradation behavior. A comprehensive parameter identification procedure and an extensive experimental validation under different operating conditions (e.g., varying C-rates, temperatures, and long-term cycling) are beyond the scope of the present study and represent a natural direction for future work.

3 Results and Discussion

The objective of analyzing these eight cell configurations is to illustrate how the proposed computational methodology can rapidly evaluate performance, thermal behavior, and aging across different design choices. The purpose of this comparison is not to identify a single optimal battery architecture, but rather to demonstrate how a unified electrochemical–thermal–aging framework can efficiently capture the coupled influence of particle size, electrode thickness, and separator geometry. In this sense, the present study should be regarded as a computational screening methodology aimed at identifying limiting trends and design trade-offs, thereby guiding future experimental investigations and cell optimization efforts.

This study serves as a methodological demonstration, showing how trends in capacity retention, thermal behavior, and SEI growth emerge as a function of electrode thickness, separator thickness, and active material particle size. By doing so, designers and experimenters can identify promising configurations before committing to large-scale testing, thereby reducing experimental effort while still gaining insight into the relative effects of key structural parameters.

In this study, eight different cell configurations of a lithium-ion battery (see Table 1) have been analyzed. The chosen materials are graphite and NMC811 for the anode and cathode layers, respectively. A liquid electrolyte ($LiPF_6$) and a polymeric separator with a density of 1300 kg/m^3 have been selected.

Cell 1 was selected as the reference configuration because its active material particle radii are smaller than those typically used in commercial electrodes. This choice provides a baseline scenario in which lithium-ion transport and electrochemical kinetics are minimally limited by particle size, allowing a clear evaluation of the influence of particle diameter and electrode thickness on performance, aging, and thermal behavior. Larger particle sizes, corresponding to commercial materials, were introduced in Cells 2 and 4 to enable a systematic comparison between an idealized configuration and realistic electrode morphologies. This approach clarifies the effect of particle size on performance trends while demonstrating the utility of the computational method: rather than experimentally testing hundreds of potential combinations, the model allows rapid screening and comparison of multiple cell designs. Therefore, the goal of these simulations is not to find a single optimal design but to show how the methodology can guide future experimental or industrial design efforts efficiently by predicting performance, degradation, and thermal behavior across a wide range of configurations.

Cells 5–8 extend the range of structural variations considered in this study by combining different electrode and separator thicknesses with the two characteristic particle sizes. Specifically, Cells 5 and 7 adopt the thinner separator of 12 μm, maintaining the anode and cathode thicknesses of 55 μm and 40 μm, respectively, while Cell 5 retains the smaller particle radii and Cell 7 incorporates the larger, commercially relevant sizes. Conversely, Cells 6 and 8 use thicker separators of 30 μm and electrode thicknesses of 135 μm for the anode and 87.5 μm for the cathode, mirroring the 4680 cylindrical cell geometry, with Cell 6 featuring the smaller particle radii and Cell 8 the larger ones. This systematic combination of particle size and layer thickness across all eight cells allows for a comprehensive evaluation of the interplay between electrode morphology, separator geometry, and electrochemical performance, providing a thorough basis for comparing capacity retention, rate capability, and thermal behavior.

Furthermore, while only two particle size values were considered in this study, this selection effectively highlights the main trend between smaller, idealized particles and larger, commercially relevant particles across all cell configurations. The comparison between these two particle sizes already provides useful guidance for experimental planning, as it captures the maximum expected impact of particle size on performance and aging. Introducing additional particle sizes would not fundamentally change the observed trends but could be pursued in future work to explore intermediate cases if desired.

3.1 Electrochemical Characterization. Initially, the charging and discharging profiles at different C-rates have been determined; the results regarding each of the eight cells at different C-rate conditions are reported in Fig. 3.

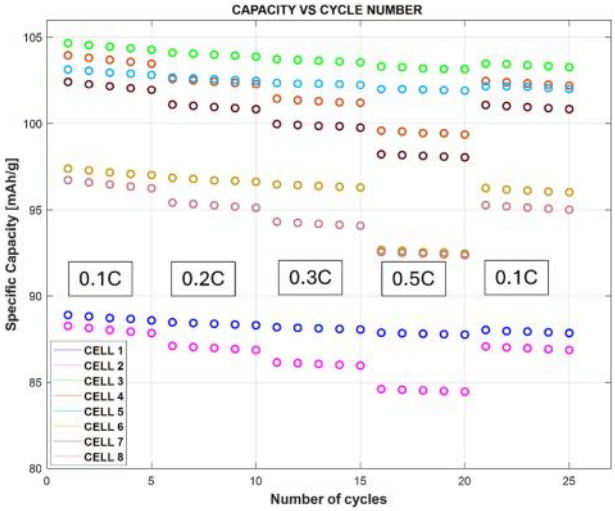

Fig. 3 Charging and discharging profiles (*y*-axes) at different C-rates for each simulated cell as a function of cycle number (*x*-axes)

Figure 3 presents a graph depicting the relationship between specific capacity (measured in mAh/g) and the number of cycles for eight different cells, labeled Cells 1–8, where the *x*-axis represents the number of cycles, while the *y*-axis quantifies specific capacity. The plot is segmented into different cycling rates, namely 0.1C, 0.2C, 0.3C, 0.5C, and 0.1C, indicating variations in charge/discharge currents throughout the cycling process. The results reveal a clear trend in capacity retention. Cells 3, 4, 5, and 7 exhibit the highest specific capacities across the range of C-rates, demonstrating superior electrochemical performance. This high baseline capacity is heavily driven by optimized layer geometries and minimized separator thicknesses. Conversely, Cells 1 and 2 show the lowest specific capacities, while Cells 6 and 8 occupy an intermediate position. This overall hierarchy reflects the complex interplay between particle size, electrode thickness, and separator volume fractions.

At elevated C-rates, the capacity fade is more pronounced in Cells 2, 4, 6, and 8, highlighting the effect of larger particle sizes and thicker electrodes on transport limitations. Conversely, Cells 1, 3, 5, and 7 maintain more stable capacities under high-rate conditions, confirming the benefit of reduced diffusion paths and optimized layer thicknesses. Overall, the figure illustrates how electrode morphology and layer configuration govern cycling stability and energy retention, providing a comprehensive comparison across all eight cell designs.

The simulations conducted in this study consider solid-state diffusion as a key mechanism influencing the performance of lithium-ion batteries with different particle sizes and separator thicknesses. The boundary conditions were set to ensure a homogeneous comparison across different configurations, maintaining consistent parameters except for the key variables under investigation. The porosity of the electrodes, an essential parameter affecting ion transport and filling behavior, was incorporated into the model and requires further refinement to ensure accurate mass calculations. Specifically, volume fractions of the negative and positive electrodes were set to 0.384 and 0.42, respectively, based on experimentally relevant values present in the literature [7].

Furthermore, it should be noted that the separator domain within this P2D framework is treated using homogenized macroscopic transport properties equivalent to the bulk electrolyte. While this simplification effectively captures the primary geometric and volumetric scaling trends, specifically how minimizing inactive separator volume shifts the cell-wide mass balance and boosts specific capacity, it does not explicitly decouple individual separator microstructural parameters such as localized porosity, tortuosity, and Bruggeman-corrected effective diffusivity. Consequently, the conclusions regarding separator optimization herein emphasize architectural and volumetric effects rather than microscopic ion transport dynamics, which remain a subject for future model refinements.

The model captures the impact of particle size on capacity retention at high C-rates, suggesting that smaller particles enhance performance due to more efficient solid-state diffusion. The ability of the model to simulate these effects aligns well with experimental trends observed in commercial cells.

The retention of capacity at high C-rates is superior for cells with smaller active material particles, confirming that solid-state diffusion plays a significant role in mitigating performance loss. This phenomenon is well captured by the simulation, which accurately reflects the differences observed between cells with varying particle diameters. Cells 2 and 4 exhibit distinct behaviors, likely due to differences in electrode filling. The assumption of complete filling leads to an underestimation of mass, introducing an error of approximately 30% in mass calculations, which should be corrected by incorporating porosity values explicitly into MATLAB-based postprocessing.

A key observation is that Cell 4 exhibits superior specific capacity compared to Cell 1, despite the latter possessing smaller, idealized electrode particles. Since this study maps the boundary conditions of the design space via a full-factorial combination matrix, Cell 1 and Cell 4 differ across all three structural dimensions: Cell 1 pairs thin electrodes (55/40 μm) and small particles with a thick separator (30 μm), whereas Cell 4 utilizes thick electrodes (135/87.5 μm) and larger commercial particles with a thin separator (12 μm).

The superior performance of Cell 4 is a direct consequence of a coupled architectural synergy. Cells 1, 2, 5, and 7 incorporate a separator that is approximately twice as thick as that of Cells 3, 4, 6, and 8. Based on internal volume and mass fraction considerations, this thick separator leads to a net capacity reduction of approximately 10% for Cell 1, where the separator constitutes a significant portion of the cell assembly. In contrast, in Cell 4, the combination of thick electrodes and a thin separator drastically reduces the inactive material volume fraction, maximizing active material loading.

Therefore, Cell 4 represents a currently mass-produced, gigascale-optimized design where the architectural benefits and the geometrical mitigation of inactive materials successfully overpower the solid-state diffusion and transport limitations typically imposed by its larger particle size.

This study provides insights into the key parameters that have driven the optimization of lithium-ion batteries, particularly in commercial cells. The results highlight the importance of separator thickness, particle size, and solid-state diffusion in determining performance, especially at high C-rates. While the absolute values of specific capacity may be underestimated due to the simplifications in the model, the primary goal was to ensure a homogeneous comparison across different configurations.

Starting from these studies performed at different C-rates for each cell, it was possible to obtain the values of specific energy and specific power by applying Eqs. (1) and (2). Subsequently, these values have been plotted in a Ragone diagram, where the working region of LIBs is reported as an area (in dark green), as can be seen in Fig. 4 [32].

From the data presented in Fig. 4, it is apparent that Cells 3, 4, 5, and 7 exhibit superior performance across the spectrum of C-rates investigated, demonstrating both high specific energy and specific power. Cells 1 and 2 show moderate performance, while Cells 6 and 8 display the lowest values in both energy and power, reflecting the impact of larger particle sizes and thicker electrodes on mass transport and solid-state diffusion limitations. Despite these differences, all cells follow the same general trend, thereby attesting to the predictive fidelity of the P2D modeling framework [33]. Particularly noteworthy are the markedly more vertical discharge curves of Cells 3, 4, 5, and 7 in the Ragone diagram, indicating

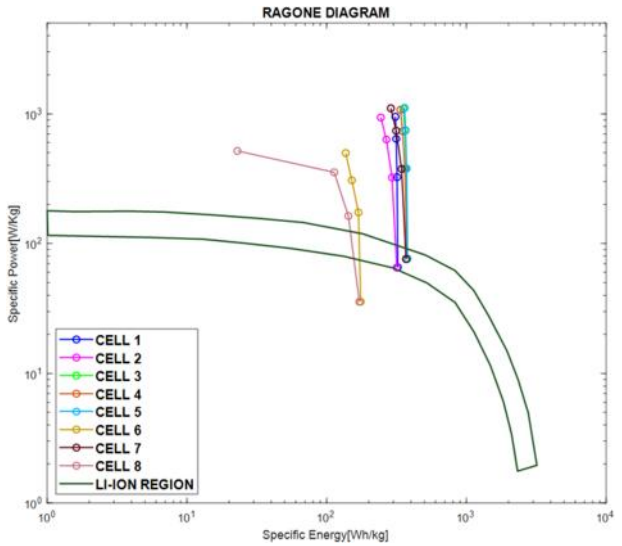

Fig. 4 Ragone plot comparing the performance of the eight simulated battery cells in terms of specific power (W/kg) versus specific energy (Wh/kg). The data points for each cell are shown in distinct colors, while closed curve represents the area of the general performance region of Li-ion batteries.

superior capacity retention, which can be ascribed to the exceptionally fine active material particles (on the order of 2.5 μm for the anode and 0.25 μm for the cathode in Cells 3 and 5, and similarly small dimensions in Cells 4 and 7). These reduced characteristic diffusion lengths alleviate solid-state transport limitations, rendering this group of cells the most "ideal" embodiments among those considered. Although the synthesis of such nanoscale particulate architectures entails greater complexity and manufacturing expense, especially in the case of Cells 3 and 5, the electrochemical advantages are manifest. It should be noted that, while all cells appear within the high-energy-density sector of the Ragone plot, the inherent inability of this portrayal to capture the inevitable decline in specific energy under realistic cycling conditions leads to an overestimation of retained capacity. This divergence primarily reflects nonidealities stemming from mass-transport constraints omitted or simplified in the model. Nonetheless, even under these conservative assumptions, the cells demonstrably uphold high-energy-density performance, underscoring their viability for practical applications.

Cell 1 was selected as a reference configuration because its active material particle radii are smaller than those typically used in commercial electrodes. This choice provides a baseline scenario in which lithium-ion transport and electrochemical kinetics are minimally limited by particle size, allowing a clear evaluation of the influence of particle diameter, electrode thickness, and separator geometry on performance, aging, and thermal behavior. Larger particle sizes, corresponding to commercial materials, are represented in Cells 2, 4, 6, and 8, enabling a systematic comparison between idealized configurations (Cells 1, 3, 5, and 7) and more commercially representative electrode morphologies.

The selection of small particle sizes in Cells 1, 3, 5, and 7 represents an idealized scenario intended to minimize solid-state diffusion limitations. The goal is not to model a commercially optimized cell but to provide benchmarks that clearly illustrate the effects of particle size, electrode thickness, and separator geometry on rate capability, heat generation, and long-term stability. By comparing these idealized configurations with cells employing larger particles and different layer thicknesses (Cells 2, 4, 6, and 8), it is possible to quantify performance differences and highlight the influence of structural and morphological parameters on electrochemical and thermal behavior.

The aim of this approach is not to identify a single optimal cell design, but rather to demonstrate how the computational method can efficiently evaluate the effects of key parameters. This comparison reveals the main trends in capacity, power, and thermal behavior, providing meaningful guidance for experimental work by showing the maximum expected impact of particle size, layer thickness, and separator geometry without the need for exhaustive testing across all possible configurations. In this sense, the methodology offers a rapid and cost-effective tool to screen multiple cell designs and inform future experimental or industrial optimization efforts.

3.2 Temperature Evaluation. In the field of electrochemical cell thermal modeling, three-dimensional (3D) simulations are widely recognized for their ability to capture realistic temperature distributions. However, the 1D case presents distinct characteristics that warrant attention. Due to the extremely small thickness involved, temperature variations in 1D models are often negligible and practically unmeasurable. From a physical perspective, heat transfer is inherently a multidimensional process; nevertheless, in 1D modeling, it becomes a theoretical abstraction, as heat is assumed to propagate in a single direction within an almost infinitesimal thickness. This simplification, while useful for analytical and computational efficiency, limits the accuracy of thermal predictions in practical applications.

Given the one-dimensional nature of the thermal coupling and the small absolute temperature variations simulated ($\sim$1 K), these thermal results are intended strictly for a relative, comparative assessment of volumetric heat-generation trends across the various electrode architectures. They do not represent absolute cell-level thermal safety limits or multidimensional thermal stability boundaries, which would require advanced 3D thermal modeling and experimental validation under abusive operational profiles.

However, the aim of this study is not to focus on 3D temperature distribution, but rather to delve into a closely related topic: the mechanisms behind cell aging, specifically the generation of heat. The key issue addressed in this work is the intrinsic heat generation within the electrodes themselves and not the thermal transport between cell layers. Indeed, certain electrode architectures are more predisposed than others to generate heat during operation. In this context, the focus is not on the absolute value of the temperature reached but rather on the relative trend of heat generation. This trend provides critical insights into the mechanisms influencing the cell aging phenomenon. Thus, the study intentionally avoids making conclusions about the heating of the complete cell, as a thorough understanding of this phenomenon would require a fully meshed and subsequently solved 3D model.

Electrode thickness plays a critical role in determining the thermal behavior of lithium-ion cells. Thicker electrodes, typical of high-energy cell designs, are associated with higher internal resistance and reduced radial heat conductivity. This structural characteristic leads to increased heat generation during discharge, particularly at elevated C-rates, and results in higher maximum surface temperatures. As stated by Waldmann et al. [34], a clear correlation emerges between total electrode layer thickness (including anode, cathode, and separators) and the temperature rise per unit C-rate. As electrode thickness increases, heat dissipation becomes less effective, and temperature gradients within the cell become more pronounced. These thermal effects are further intensified by the corresponding increase in internal resistance, which limits the rate capability of the cell and accelerates temperature rise under load; even when temperature response is normalized to cell capacity, the distinction between high-energy and high-power formats becomes less pronounced, indicating that thermal sensitivity is driven more by structural parameters such as electrode thickness than by energy content alone. This relationship introduces a design trade-off: while thicker electrodes enhance energy density, they also compromise thermal performance, leading to localized thermal stress at high discharge rates. Effective

thermal management strategies and careful optimization of electrode geometry are therefore essential to ensure both high performance and to mitigate volumetric heat generation in advanced lithium-ion battery systems [34].

The core of this research lies in comparing the heat-generation terms to identify the relative trends that drive aging mechanisms. This approach enables a deeper understanding of localized thermal behavior without the need for a comprehensive 3D model of the entire cell geometry.

Figure 5 comprises two subplots that illustrate the interplay between temperature, current, and voltage over time during two charging and discharging cycles. The data shown correspond to simulations performed on Cell 1. Figure 5(*a*) presents the temperature evolution in Kelvin as a function of time, measured in seconds. Notable sharp changes occur around 8000 s when the charging phase is completed, and the discharging part of the cycle begins. As can be seen, the cell temperature increases moderately during the CC charging phase and then decreases gently during the CV charging phase. During the initial phase of CC discharging, the temperature appears to have a small bump, which becomes a noticeable peak in the final phase of discharging. The temperature, represented by a blue curve, remains largely stable with minor oscillations, ranging from approximately 293.15 K to 293.3 K. This temperature variation range is compact because of the thicknesses accounted for in the 1D model, in the order of micrometers, and in sight of the cooling system approximated by the heat transfer coefficient $h = 10$ which results in a great amount of heat transferred through the two extreme points of the cell.

Figure 5(*b*) depicts the temporal behavior of current and voltage. The current, shown as a solid line, varies between −20 A and +20 A depending on the specific phase of charging or discharging (CCCV charging and CC discharging). The phases previously mentioned are clearly identifiable even in the voltage subplot, represented by a dashed line, which exhibits a smooth variation within a range of 2.5 V to 4.1 V. The relationship between the subplots highlights the interdependence of electrochemical and thermal dynamics; in fact, the temperature profile corresponds to certain transitions in current and voltage.

To have a clearer reading of the results, Fig. 6 represents the interpolation of the temperature peaks at every cycle for each cell. As highlighted in the graph, the micrometer thicknesses of anode, separator, and cathode layers and the introduction of the heat transfer coefficient $h = 10$ in each cell analyzed imply an overall temperature variation, which oscillates in a range of about 1 K.

Figure 6 presents the long-term trends in maximum temperature over repeated cycling for all eight cells in a single-plot format, emphasizing heat generation rather than instantaneous temperature peaks. The data reveal distinct thermal behaviors depending on particle size and electrode/separator configuration. Cells 4 and 8 exhibit the highest maximum temperatures, reaching approximately 294.3 K, indicating significant cumulative heat generation due to larger active material particles and thicker electrodes. Cells 2 and 7 display a similar temperature trend but with lower absolute values, while Cells 3 and 6 show moderately elevated yet relatively stable temperatures. Finally, Cells 1 and 5 maintain the lowest maximum temperatures, with minimal growth over repeated cycles. This hierarchy highlights the influence of particle size and layer geometry on solid-state lithium diffusion and internal resistance: larger particles and thicker electrodes impede ion transport, promoting heat buildup, whereas smaller particles and optimized layer thicknesses facilitate efficient diffusion, mitigating temperature rise and reducing relative heat-generation rates.

The complete temperature profiles (see Fig. 12) exhibit periodic oscillatory behavior, where each cell shows cyclic increases and decreases in temperature depending on the specific phase of the charging/discharging cycle (CCCV charging and CC discharging). The maximum cell temperature rises steadily but at different rates across all eight cells. Overall, the temperature trends indicate a gradual increase over repeated cycling, reflecting the cumulative accumulation of heat throughout the battery life. Despite similarities in the oscillatory patterns, the amplitude and growth of temperature fluctuations vary significantly among the cells: Cells 4 and 8 reach the highest temperatures, Cells 2 and 7 show moderate peaks, Cells 3 and 6 are slightly elevated yet stable, and Cells 1 and 5 maintain the lowest and most stable temperature profiles. This variation underscores the combined influence of particle size,

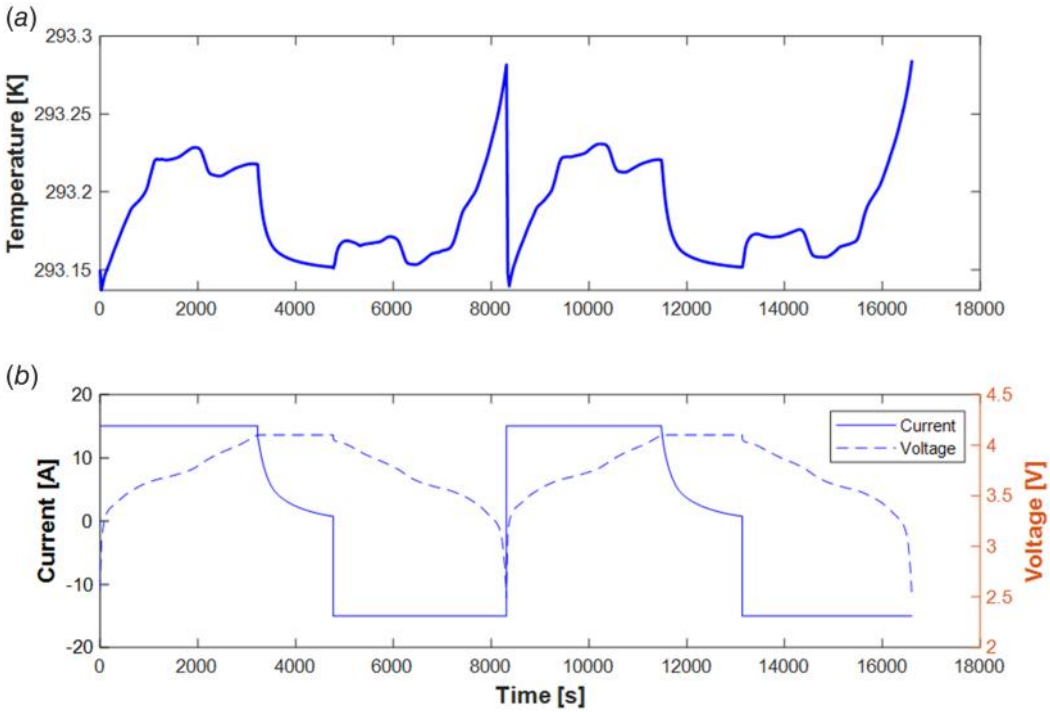

Fig. 5 (*a*) Temperature profile during CCCV charging and CC discharging. (*b*) Selected cell voltage profile and current.

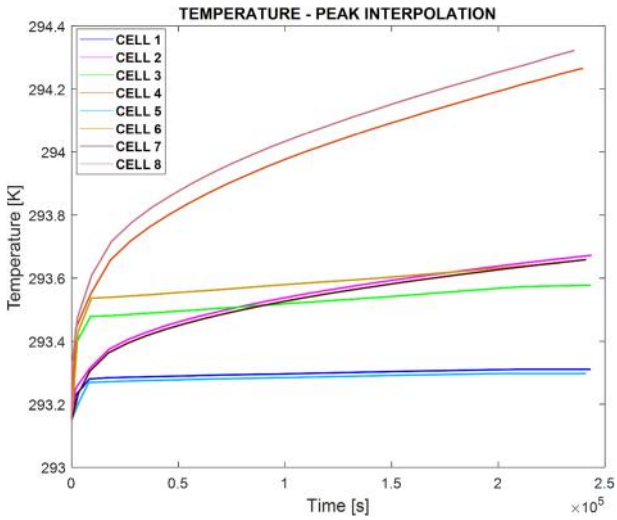

Fig. 6 Interpolation of the temperature peaks over 2500 cycles

electrode thickness, and separator geometry on overall heat generation and solid-state lithium diffusion.

3.3 Capacity Retention. Figure 7 illustrates the capacity fade of the cells subjected to a 1C cycling regime, where the charge and discharge rate equals the nominal capacity. The graph depicts relative capacity retention, expressed as a percentage of the initial capacity on the *y*-axis, as a function of the number of cycles on the *x*-axis, ranging from 0 to 2500.

The initial capacities of the eight cells differ due to variations in electrode thickness and particle size. In particular, Cells 1, 2, 5, and 7 have an initial specific capacity of approximately 89 mAh/g, while Cells 3, 4, 6, and 8 exhibit higher initial capacities around 105 mAh/g.

All cell behaviors exhibit a progressive decline in capacity with increasing cycle count, indicating typical aging behavior. However, the rate of degradation varies among the cells. Cell 1 demonstrates the slowest capacity fade, maintaining roughly 85% of its initial capacity after 2500 cycles. Cells 3, 5, 6, and 7 follow with intermediate fading rates, showing relatively stable retention over the cycles. Cells 2 and 4 experience the most pronounced degradation, with Cell 4 dropping to approximately 70% of its initial capacity, while Cell 8 shows intermediate behavior between the top-performing and worst-performing groups.

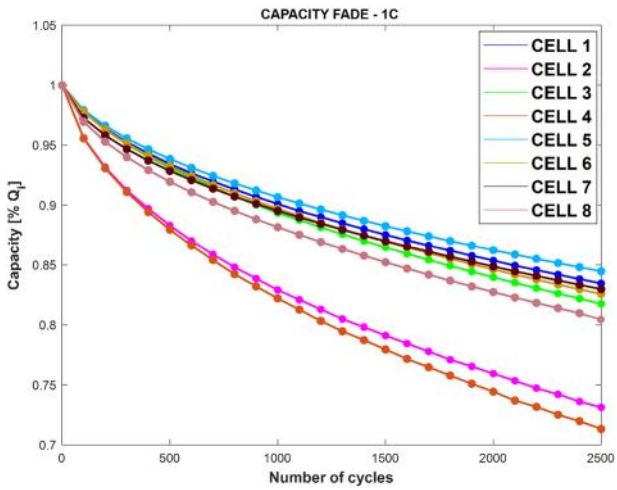

Fig. 7 Capacity fade occurring in 2500 charge/discharge cycles at 1C rate

This hierarchy reflects the interplay between particle size, electrode thickness, and separator geometry. Larger particle diameters enhance solid-state diffusion pathways but also lead to greater polarization within the electrodes. According to the Butler–Volmer equation, increased polarization accelerates the formation of the SEI. As the SEI grows, it introduces additional resistance at the electrode–electrolyte interface, further increasing polarization. This self-reinforcing degradation mechanism accelerates over time, ultimately reducing cycle life and overall performance stability.

3.4 Differential Capacity Analysis. Differential capacity analysis (DCA), also referred to as incremental capacity analysis (ICA), is a commonly employed method to investigate the processes occurring within battery electrodes during constant-current charging or discharging. It is defined as the rate of change of charge with voltage (dQ/dV), where the peaks observed in the ICA are attributed to plateaus in the voltage profile and are indicative of phase transitions in the active electrode material caused by intercalation [35]. Initially introduced in the late 1960s, ICA has become an established technique for noninvasive performance assessment of lithium-ion batteries. In recent years, efforts have focused on establishing direct correlations between changes in ICA peaks and battery degradation mechanisms to enhance the management of SOH [36].

The electric charge $Q(t)$ is determined by integrating the current $I(t)$ over time t, using the trapezoidal rule. This calculation involves N measured data points, starting from the initial time ($i=1$) to a specific time tf ($f=N$); this method is accurate when the dataset comprises small, equidistant time intervals. By convention, charging currents are positive ($I>0$), while discharging currents are negative ($I<0$). The differential capacity ($C=dQ/dV$), representing capacitance (C), is obtained by numerically differentiating the electric charge $Q(t)$ with respect to the instantaneous voltage $V(t)$ using the straightforward differential method [37].

As shown in Fig. 8(*a*), the voltage ranges up to 3.8 V remain stable, displaying two anodic peaks between 3.4 V and 3.8 V. These peaks are attributed to lithium insertion into the anode and the phase transition from a hexagonal to a monoclinic (H1◇M) lattice structure in the NCM [38]. At voltages higher than 3.8 V, the NMC811 curve deviates from them, showing an anodic characteristic at about 3.9 V related to the M◇H2 phase transition. Looking at the higher voltage region, at about 4.1 V, a more pronounced peak appears, belonging to the H2◇H3 phase transition. For these reasons, it has been decided to cycle the graphite–NMC811 cell in the range of 2.5–4.1 V, so that the last described peak could be visible.

Figure 8(*b*) presents a differential capacity analysis (dQ/dV) performed at C/5 for the cells studied at the 2500th cycle. The *x*-axis represents the voltage (V), while the *y*-axis corresponds to the differential capacity (dQ/dV) in Ah/V. The curves highlight the electrochemical behavior of each cell, showcasing variations in peak positions and intensities with respect to the first cycle (as shown in Fig. 8(*a*)), which indicate differences in aging mechanisms, reaction kinetics, and phase transitions within the electrodes. Furthermore, discrepancies among the four cells suggest varying degradation pathways, mainly due to the differences in material properties (specified in Table 1).

Peak shifting in ICA occurs due to resistive and diffusion polarization effects, which become more pronounced at higher charge/discharge rates (C-rates). These effects shift the peak locations to higher voltages during charging and lower voltages during discharging. Additionally, higher C-rates increase concentration gradients within the electrodes and reduce relaxation times for phase equalization, leading to broader peaks with reduced magnitudes, which further impacts their diagnostic resolution [36].

In particular, charging peaks tend to shift to higher voltages, a result of increased overpotentials, while discharging peaks move

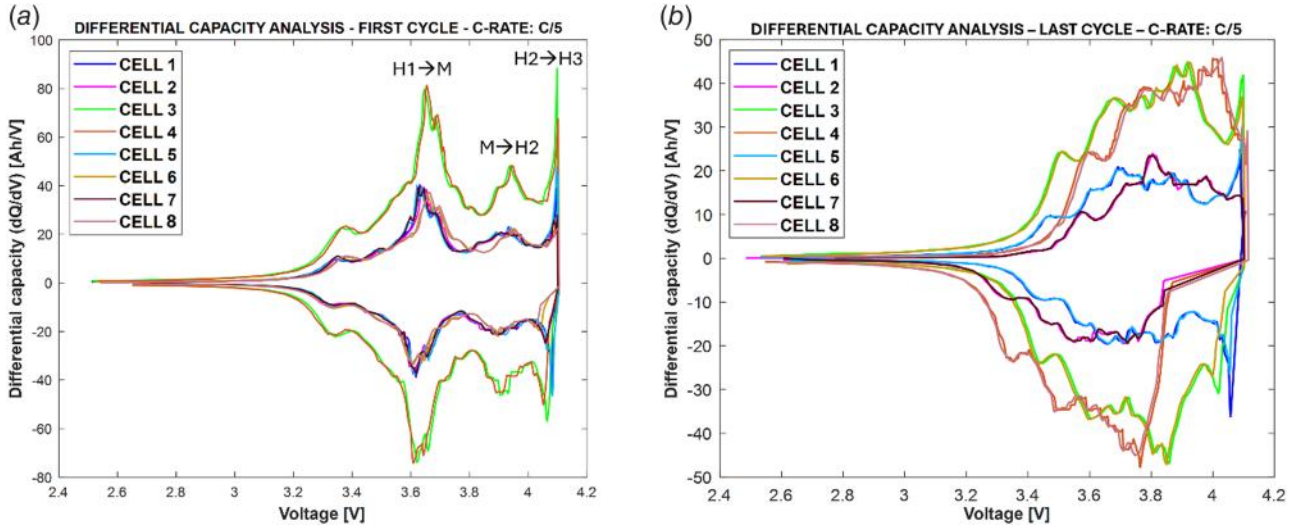

Fig. 8 (*a*) Differential capacity (*dQ/dV*) plot of the four different cells after the first cycle, as a function of voltage (*V*). (*b*) Differential capacity (*dQ/dV*) plots of the four different cells after 2500 cycles, as a function of voltage (*V*).

to lower voltages, reflecting reduced ionic mobility and growing kinetic limitations. Simultaneously, the overall intensity of the peaks diminishes, indicating a loss in electrochemical activity and a decline in usable capacity. Moreover, specific changes in the shape and amplitude of the peaks can provide insights into the underlying degradation mechanisms. For example, a noticeable reduction in the peak near 3.6 V may suggest lithium plating or anode deterioration, whereas a general suppression of all peaks could point to cathode degradation or structural disintegration such as electrode delamination [37].

3.5 Cells' Comparison. To evaluate the volume of the different components present in a cell depending on the thickness of the three layers reported in Table 1, a 18650 cylindrical cell format (diameter = 18 mm and height = 65 mm) has been considered. Four different combinations of layer thicknesses (Cells 1 and 2, Cells 3 and 4, Cells 5 and 7, and Cells 6 and 8, respectively) have been adopted to fill this cell format, while keeping the thickness of the positive and negative current collectors fixed at 12 μm and 6 μm, respectively. The analysis was performed using a 3D CAD model representing only the *jellyroll* portion of the cell, in which the thicknesses of the individual layers were varied to assess how different configurations affect the overall mass distribution of the internal components.

Table 4 summarizes the results collected for what concerns the mass of the different components considered, measured in m^3. Those values are reported in graphs in Fig. 1, in which the volumes of the components of the cells are reported as a percentage of the total volume.

Figure 9 presents a comparative analysis of the volumetric composition of four groups of lithium-ion battery cells, Cell 1 and Cell 2, Cell 3 and Cell 4, Cell 5 and Cell 7, and Cell 6 and Cell 8, illustrated through pie charts. The volumes of the various layers were directly obtained from the 3D CAD models and subsequently multiplied by their respective densities to calculate the mass contributions of each component.

For Cell 1 and Cell 2 (Fig. 9(*a*)), the total mass is predominantly occupied by the positive electrode (48%) and the negative electrode (31%), followed by the separator (10%). The positive current collectors and negative current collectors contribute marginally to the overall volume, accounting for 4% and 7%, respectively. In contrast, Cell 3 and Cell 4 (Fig. 9(*b*)) exhibit a different distribution, with the positive electrode constituting the largest fraction at 54%, and the negative electrode occupying an even greater share at 38% with respect to the other case. The separator volume is reduced to 2%, while the positive and negative current collectors are further minimized to 2% and 4%, respectively.

For Cell 5 and Cell 7 (Fig. 9(*c*)), the volumetric analysis shows a reduced separator fraction of approximately 4%, lower than that of Cells 1 and 2, which consequently allows the active electrode layers to occupy a larger proportion of the total volume. In particular, both the positive and negative electrodes show increased percentages compared to the first pair, enhancing the potential energy density of these configurations. The contributions of the current collectors remain similar to those of previous cases, maintaining a minimal impact on overall volume.

By contrast, Cells 6 and 8 (Fig. 9(*d*)) exhibit a higher separator fraction compared to Cells 3 and 4 yet still achieve a well-balanced distribution among all layers. The positive and negative electrodes, together with the separator and current collectors, are proportioned in a way that optimizes structural and electrochemical balance, offering an improved volumetric arrangement compared to Cells 1 and 2.

This figure underscores the architectural differences between the two cell configurations, with Cell 3 & 4 favoring a higher active material content, particularly in the negative electrode, at the expense of separator and current collector mass fractions, potentially enhancing energy density.

Table 2 presents the calculated energy and power values for the cell configurations when implemented in the cylindrical 18650 format. These values were obtained by scaling the corresponding specific energy and specific power metrics, previously derived from the discharge voltage profiles and illustrated in the Ragone plot (Fig. 4), by the total mass of the cell in each configuration. The total cell mass was determined by accounting for the contributions of the principal components, namely the anode, cathode, separator, and current collectors, taking into consideration their respective material densities and mass fractions within the complete cell architecture, as detailed in Fig. 9.

Cells 1 and 2 exhibit similar energy outputs of 13.69 Wh and 13.47 Wh, respectively, and comparable power values of 2.78 W and 2.74 W. Likewise, Cells 3 and 4 display closely match energy values of 15.66 Wh and 16.58 Wh, along with power outputs of 3.22 W and 3.41 W. The similarity observed between Cell 1 and Cell 2, as well as between Cell 3 and Cell 4, is attributed to their identical layer thickness; the only variation lies in the particle sizes of the active materials in both the anode and cathode. These results suggest that, while particle size has a measurable

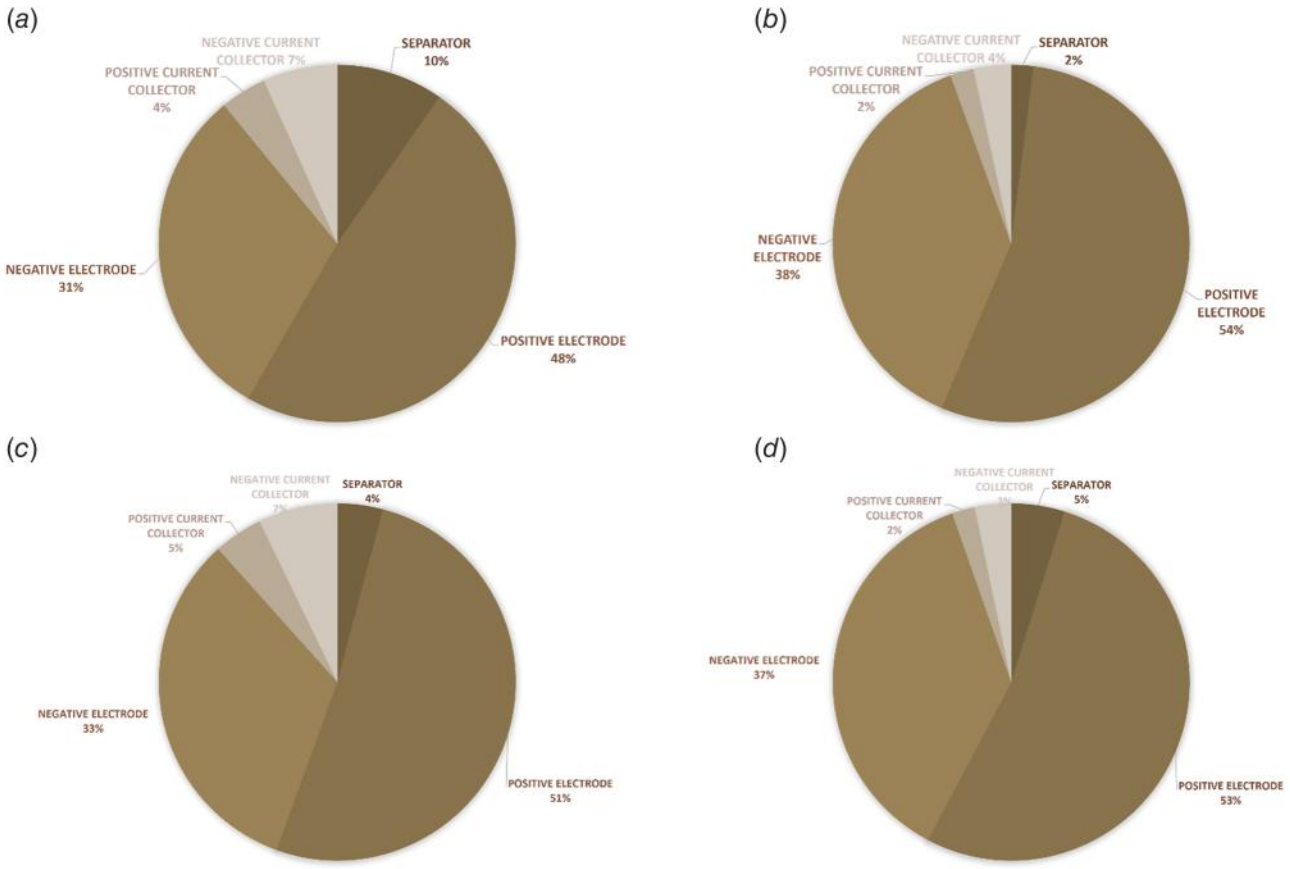

Fig. 9 Mass distribution of battery cell components across (*a*) Cell 1 and Cell 2, (*b*) Cell 3 and Cell 4, (*c*) Cell 5 and Cell 7, and (*d*) Cell 6 and Cell 8

impact on performance, electrode thickness plays a more dominant role in determining the overall energy and power capabilities of the cell.

Cells 5 and 7 exhibit energy outputs of 17.61 Wh and 17.19 Wh, with corresponding power values of 3.54 W and 3.53 W. By contrast, Cells 6 and 8 present lower energy values of 7.41 Wh and 7.25 Wh, and power values of 1.51 W for both, differing from Cells 5 and 7 primarily due to the larger particle sizes of the electrode materials.

A significant trend in lithium-ion battery development over the past two decades has been the progressive reduction in the thickness of key cell components, including the anode and cathode current collectors, separators, and electrode foils. Between 2010 and 2030, the separator thickness is projected to decline from 25 μm to 5 μm, a reduction that enhances specific energy density by increasing the volume available for active materials. Similarly, cathode foil thickness has been reduced from 30 μm to 6 μm, and anode foil thickness from 21 μm to 6 μm during the same period. These changes not only lower material costs but also contribute substantially to improvements in cell-level energy density and cost efficiency. The driving force behind these advancements includes both technological innovations in manufacturing processes and the imperative to reduce the cost and weight of LiBs for electric vehicle applications. However, achieving ultra-thin dimensions presents challenges in mechanical stability and scalability, indicating that further improvements will require concurrent advances in materials engineering and production technology [39].

The progressive thinning of separators in lithium-ion batteries reflects a deliberate strategy to minimize the proportion of inactive materials within the cell architecture. By reducing separator thickness, manufacturers can decrease internal cell resistance, thereby improving ion transport and overall electrochemical performance. In parallel, the mass fraction of both electrodes has increased, with the anode and cathode exhibiting approximate rises of 7% and 6%, respectively. These increases indicate a design shift toward architecture optimized not only for higher energy density but also for improved performance under fast-changing conditions. In particular, a higher anode mass fraction helps suppress lithium plating during high-rate charging, contributing to enhanced cell stability and safety. As illustrated in Fig. 9, the increasing contribution of the negative electrode follows the prevailing industrial trend, reflecting a growing emphasis on robustness and efficiency in next-generation cell designs.

The results of this study demonstrate that different battery performance characteristics are governed by distinct physical parameters of the electrode materials. Specifically, properties such as aging behavior and DCA profiles are strongly influenced by the particle diameter of the anode and cathode active materials, as evidenced by the trends observed in the corresponding results. In contrast, characteristics related to energy and power performance are more directly affected by electrode thickness. This distinction emphasizes the need to separately optimize both particle-scale and electrode-scale design parameters to achieve targeted improvements in lithium-ion battery performance. The decoupling of these effects offers a valuable framework for guiding future cell engineering strategies aimed at balancing long-term durability with high energy and power densities.

4 Conclusions

This study provided a detailed analysis of the electrochemical performance and aging mechanisms of LIBs with varying cell

configurations. Key design parameters, such as electrode thickness, active material particle size, and separator dimensions, were shown to significantly influence energy density, cycle life, and heat generation. P2D simulations confirmed that smaller particle sizes improve lithium-ion transport at high C-rates, while thinner separators enhance specific capacity by reducing inactive mass. However, thicker electrodes, despite increasing energy density, lead to greater heat accumulation, potentially accelerating degradation, highlighting the need for careful architectural trade-offs.

Quantitative results showed that Cells 5 and 7 achieved the highest energy and power outputs (17.61 Wh and 3.54 W for Cell 5; 17.19 Wh and 3.53 W for Cell 7), followed closely by Cells 3 and 4 (15.66–16.58 Wh and 3.22–3.41 W). Cells 1 and 2 exhibited moderate values (13.47–13.69 Wh and 2.74–2.78 W), while Cells 6 and 8 had the lowest energy and power (7.25–7.41 Wh and 1.51 W), reflecting the influence of larger particle sizes in these configurations. This ranking highlights the combined effects of electrode thickness and active material particle size on cell performance, illustrating the trade-off between maximizing energy and power and maintaining favorable structural and thermal characteristics.

DCA revealed structural and electrochemical changes after extended cycling, while thermal modeling highlighted the influence of electrode geometry on heat generation. Although the simulations were performed at the electrode scale and relied on material properties adopted from literature, the application of identical boundary conditions provided a consistent and homogeneous basis for comparing the different cell configurations.

Overall, the proposed computational approach represents an effective and low-cost tool for electrode architecture optimization, enabling rapid design screening and reducing the need for extensive experimental work. These findings underscore the importance of multiscale optimization in next-generation lithium-ion battery design, where balancing high performance and long-term stability remains critical.

Finally, this work demonstrates that a one-dimensional P2D framework represents an effective tool for the rapid evaluation of multiple lithium-ion battery configurations, highlighting how particle size, electrode thickness, and separator geometry influence electrochemical performance, thermal response, and aging behavior. Despite the inherent simplifications of the model, the proposed electrochemical–thermal–aging framework is capable of capturing the main trends governing cell operation and degradation.

The principal contribution of the present study does not lie in introducing new electrochemical mechanisms, but rather in demonstrating how a unified physics-based framework can be employed as a computational screening methodology for assessing coupled design trade-offs. By enabling the simultaneous evaluation of performance, heat generation, and long-term degradation, the proposed approach provides a practical, time-efficient, and cost-effective tool for preliminary cell design and for reducing the extent of experimental campaigns required during battery development.

Since the electrochemical and thermal parameters were adopted from literature and no additional experimental calibration was performed, the results should be interpreted mainly as comparative predictions aimed at identifying relative trends and design trade-offs rather than exact quantitative forecasts. Experimental validation against full-cell measurements represents a natural continuation of the present work.

Conflict of Interest

There are no conflicts of interest.

Data Availability Statement

No data, models, or code were generated or used for this article.

Appendix

See Figs. 10–12 and Tables 3 and 4.

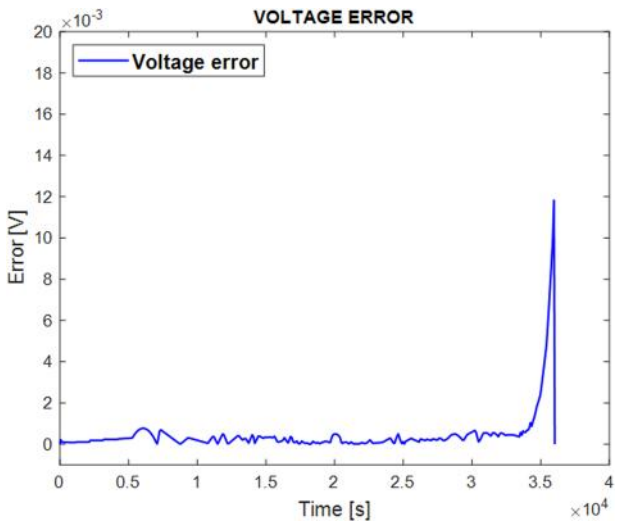

Fig. 10 Voltage error between using "normal" and "extremely fine" mesh during the first discharge cycle at 0.1C in Cell 1

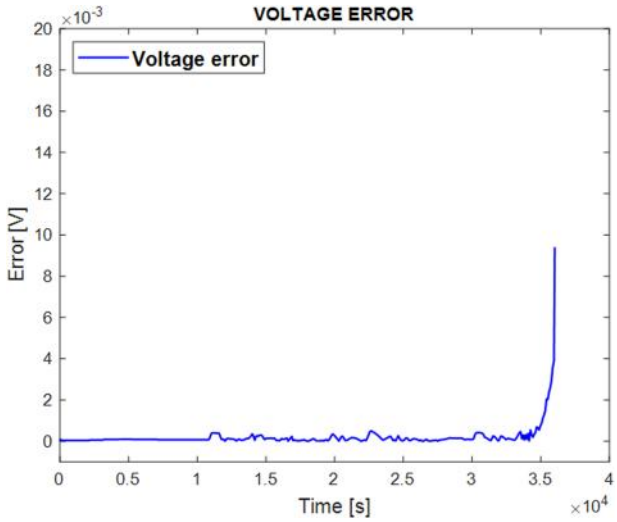

Fig. 11 Voltage error between using convergence equal to 10^{-4} and equal to 10^{-6} during the first discharge cycle at 0.1C in Cell 1

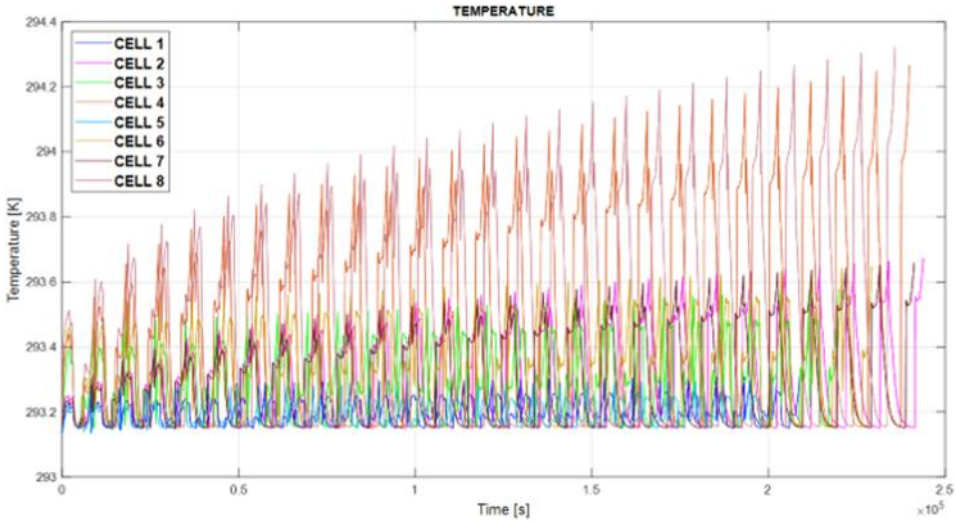

Fig. 12 Peak interpolation as a function of time for the different tested cells under study over time. Cell 1 and Cell 2 display relatively smaller oscillations, with maximum temperatures remaining close to 293.8 K. Instead, Cell 8 and Cell 6 exhibit significantly larger temperature peaks, with Cell 8 consistently reaching the highest temperatures, surpassing 294.2 K in most cycles.

Table 3 Boundary conditions, initial conditions, and modeling constraints adopted in the P2D electrochemical–thermal–aging simulations

Model	Domain/location	Condition type	Mathematical/physical description
Electrochemical (P2D)	Negative current collector ($x=0$)	Electrical boundary condition	Applied current density: $-\sigma_n\,\partial\varphi_s/\partial x = i_{app}/A$, with i_{app} determined by the imposed C-rate
Electrochemical (P2D)	Positive current collector ($x=L$)	Electrical reference	Solid-phase potential set to zero: $\varphi_s = 0$ V
Electrochemical (P2D)	Cell terminals	Voltage cutoff	Charge cutoff voltage = 4.1 V; discharge cutoff voltage = 2.5 V
Electrochemical (P2D)	Electrode–separator interfaces	Continuity condition	Continuity of electrolyte concentration c_e, electrolyte potential φ_e, and ionic flux
Electrochemical (P2D)	Solid particles ($r=0$)	Symmetry condition	$\partial c_s/\partial r = 0$
Electrochemical (P2D)	Solid particle surface ($r=R_p$)	Interfacial flux	$-D_s\partial c_s/\partial r = j_n/F$, governed by Butler–Volmer kinetics
Electrochemical (P2D)	Electrolyte at current collectors	No-flux condition	$\partial c_e/\partial x = 0$
Electrochemical (P2D)	Electrolyte potential	Charge conservation	$\partial i_e/\partial x = a_s j_n$
Electrochemical (P2D)	Initial condition	Initial lithium distribution	Uniform initial solid-phase lithium concentration corresponding to the selected initial SOC
Thermal	Entire cell	Initial condition	Uniform initial temperature: $T(x,t=0) = 293.15$ K
Thermal	External cell surfaces	Convective heat transfer	$-k\partial T/\partial n = h(T - T_{amb})$, with $h = 10$ W/m^2/K and $T_{amb} = 293.15$ K
Thermal	Internal domains	Heat generation	Volumetric heat source including reversible and irreversible contributions
Aging (SEI)	Negative electrode surface	Side reaction kinetics	SEI formation modeled via solvent reduction reaction following Ramadass et al.
Aging (SEI)	SEI thickness	Cycle-based evolution	SEI thickness updated discretely at the end of each complete charge–discharge cycle
Aging (SEI)	Film resistance	Accumulation rule	Film resistance updated cumulatively as a function of SEI thickness
Geometry	Whole cell	Dimensionality constraint	One-dimensional through-thickness P2D model; radial and axial gradients neglected
Simulation protocol	All configurations	Cycling conditions	2500 charge–discharge cycles at C-rates ranging from C/5 to 3C

Table 4 Components mass (in kg) in each of the modeled cells, evaluated considering a cylindrical 18650 cell

Configuration	Cells 1 and 2 (kg)	Cells 3 and 4 (kg)	Cells 5 and 7 (kg)	Cells 6 and 8 (kg)
Positive electrode	0.00412737	0.000896389	0.001916057	0.002045914
Negative electrode	0.020624937	0.024115753	0.023897577	0.022355248
Separator	0.01305618	0.01691949	0.01526786	0.0155986
Positive current collector	0.001777032	0.000945027	0.002067228	0.000876582
Negative current collector	0.002862865	0.001504538	0.003338365	0.001391785

References

[1] Kim, T., Song, W., Son, D. Y., Ono, L. K., and Qi, Y., 2019, "Lithium-Ion Batteries: Outlook on Present, Future, and Hybridized Technologies," J. Mater. Chem. A, **7**(7), pp. 2942–2964.

[2] Lin, C., Tang, A., and Wang, W., 2015, "A Review of SOH Estimation Methods in Lithium-Ion Batteries for Electric Vehicle Applications," Energy Procedia, **75**, pp. 1920–1925.

[3] Kim, H. J., Krishna, T. N. V., Zeb, K., Rajangam, V., Muralee Gopi, C. V. V., Sambasivam, S., Venkata-Haritha, M., and Obaidat, D., 2020, "A Comprehensive Review of Li-Ion Battery Materials and Their Recycling Techniques," Electronics, **9**(7), p. 1161.

[4] Zubi, G., Dufo-López, R., Carvalho, M., and Pasaoglu, G., 2018, "The Lithium-Ion Battery: State of the Art and Future Perspectives," Renewable Sustainable Energy Rev., **89**, pp. 292–308.

[5] Wang, F., Robert, R., Chernova, N. A., Pereira, N., Omenya, F., Badway, F., Hua, X., et al., 2011, "Conversion Reaction Mechanisms in Lithium Ion Batteries: Study of the Binary Metal Fluoride Electrodes," J. Am. Chem. Soc., **133**(46), pp. 18828–18836.

[6] Ganesh, P., Kent, P. R. C., and Jiang, D. E., 2012, "Solid-Electrolyte Interphase Formation and Electrolyte Reduction at Li-Ion Battery Graphite Anodes: Insights From First-Principles Molecular Dynamics," J. Phys. Chem. C, **116**(46), pp. 24476–24481.

[7] Comsol, 2021, "D Isothermal Lithium-Ion Battery Introduction," www.comsol.com/trademarks

[8] Ank, M., Sommer, A., Abo Gamra, K., Schöberl, J., Leeb, M., Schachtl, J., Streidel, N., et al., 2023, "Lithium-Ion Cells in Automotive Applications: Tesla 4680 Cylindrical Cell Teardown and Characterization," J. Electrochem. Soc., **170**(12), p. 120536.

[9] Zhao, R., Liu, J., and Gu, J., 2015, "The Effects of Electrode Thickness on the Electrochemical and Thermal Characteristics of Lithium Ion Battery," Appl. Energy, **139**, pp. 220–229.

[10] Kasnatscheew, J., Placke, T., Streipert, B., Rothermel, S., Wagner, R., Meister, P., Laskovic, I. C., and Winter, M., 2017, "A Tutorial Into Practical Capacity and Mass Balancing of Lithium Ion Batteries," J. Electrochem. Soc., **164**(12), pp. A2479–A2486.

[11] Bergstrom, H. K., Fong, K. D., and McCloskey, B. D., 2021, "Interfacial Effects on Transport Coefficient Measurements in Li-Ion Battery Electrolytes," J. Electrochem. Soc., **168**(6), p. 060543.

[12] Zhang, S. S., Jow, T. R., Amine, K., and Henriksen, G. L., 2002, "$LiPF_6$–EC–EMC Electrolyte for Li-Ion Battery," J. Power Sources, **107**(1), pp. 18–23.

[13] Laakso, E., Efimova, S., Colalongo, M., Kauranen, P., Lahtinen, K., Napolitano, E., Ruiz, V., et al., 2024, "Aging Mechanisms of NMC811/Si-Graphite Li-Ion Batteries," J. Power Sources, **599**, p. 234159.

[14] Santhanagopalan, S., Guo, Q., Ramadass, P., and White, R. E., 2006, "Review of Models for Predicting the Cycling Performance of Lithium Ion Batteries," J. Power Sources, **156**(2), pp. 620–628.

[15] Hashemzadeh, P., Désilets, M., Lacroix, M., and Jokar, A., 2022, "Investigation of the P2D and of the Modified Single-Particle Models for Predicting the Nonlinear Behavior of Li-Ion Batteries," J. Energy Storage, **52**(Part A), p. 104909.

[16] Jokar, A., Rajabloo, B., Désilets, M., and Lacroix, M., 2016, "Review of Simplified Pseudo-Two-Dimensional Models of Lithium-Ion Batteries," J. Power Sources, **327**, pp. 44–55.

[17] Balagopal, B., and Chow, M. Y., 2016, "Effect of Anode Conductivity Degradation on the Thevenin Circuit Model of Lithium Ion Batteries," IECON Proceedings (Industrial Electronics Conference), Florence, Italy, Oct. 24–27, IEEE Computer Society, pp. 2028–2033.

[18] Yu, Z., Tian, Y., and Li, B., 2024, "A Simulation Study of Li-Ion Batteries Based on a Modified P2D Model," J. Power Sources, **618**, p. 234376.

[19] Both, S., Börner, M., Danner, T., Börner, M., Waidhas, M., Knoblauch, V., Latz, A., and Horstmann, B., 2023, "Insights Into Performance and Degradation of Commercial Ni-Rich Cathodes: A Modeling Perspective," ECS Meeting Abstracts, Gothenburg, Sweden, Dec. 2023, Vol. MA2023-02, No. 5, p. 829.

[20] Beyers, I., Bensmann, A., and Hanke-Rauschenbach, R., 2023, "Ragone Plots Revisited: A Review of Methodology and Application Across Energy Storage Technologies," J. Energy Storage, **73**(Part B), p. 109097.

[21] Lin, X. W., Zhou, Z. F., Liu, T. F., Xue, S. Q., Liang, Y., Zhang, L. F., Liu, B., et al., 2023, "Rate Capability and Ragone Plots for Designing Battery Thermal Management System Based on Phase Change Material," J. Energy Storage, **74**(Part B), p. 109539.

[22] Kato, H., Kobayashi, Y., and Miyashiro, H., 2018, "Differential Voltage Curve Analysis of a Lithium-Ion Battery During Discharge," J. Power Sources, **398**, pp. 49–54.

[23] Krause, L. J., Brandt, T., Chevrier, V. L., and Jensen, L. D., 2017, "Surface Area Increase of Silicon Alloys in Li-Ion Full Cells Measured by Isothermal Heat Flow Calorimetry," J. Electrochem. Soc., **164**(9), pp. A2277–A2282.

[24] Luo, P., Li, P., Ma, D., Wang, K., and Zhang, H., 2022, "Coupled Electrochemical-Thermal-Mechanical Modeling and Simulation of Lithium-Ion Batteries," J. Electrochem. Soc., **169**(10), p. 100535.

[25] 1998, "Heat Transfer Module User's Guide," www.comsol.com/blogs

[26] Ramadass, P., Haran, B., Gomadam, P. M., White, R., and Popov, B. N., 2004, "Development of First Principles Capacity Fade Model for Li-Ion Cells," J. Electrochem. Soc., **151**(2), pp. A196.

[27] Hamisi, C. M., Gerutu, G. B., Greyson, K. A., and Chombo, P. V., 2022, "Thermal Behavior of Lithium-Ion Battery Under Variation of Convective Heat Transfer Coefficients, Surrounding Temperatures, and Charging Currents," J. Loss Prev. Process Ind., **80**, p. 104922.

[28] Boroujeni, S. M., and Birke, K. P., 2019, "Study of a Li-Ion Cell Kinetics in Five Regions to Predict Li Plating Using a Pseudo Two-Dimensional Model," Sustainability (Switzerland), **11**(22), p. 6392.

[29] O'Kane, S. E. J., Ai, W., Madabattula, G., Alonso-Alvarez, D., Timms, R., Sulzer, V., Edge, J. S., Wu, B., Offer, G. J., and Marinescu, M., 2022, "Lithium-Ion Battery Degradation: How to Model it," Phys. Chem. Chem. Phys., **24**(13), pp. 7909–7922.

[30] Roy, A., Movahedi, H., Siegel, J. B., and Stefanopoulou, A. G., Oct. 2023, "Empirical Modeling of Degradation in Lithium-Ion Batteries and Validation in Complex Scenarios," IFAC-PapersOnLine, **56**(3), pp. 457–462.

[31] Giusti, I., De Santis, M., Santi, G. M., and Piancastelli, L., 2026, "Thermal Modeling and Performance Evaluation of Tesla 4680 Lithium-Ion Cell," *Design Tools and Methods in Industrial Engineering V*, G. Berselli, A. O. Andrisano, P. Di Stefano, C. Rizzi, and F. Gherardini, eds., Springer Nature, Cham, Switzerland, pp. 182–193.

[32] Koten, H., and Bilal, S. B., 2018, "Recent Developments in Electric Vehicles," Int. J. Adv. Autom. Technol., **1**(1), pp. 35–52.

[33] Futscher, M. H., Brinkman, L., Müller, A., Casella, J., Aribia, A., and Romanyuk, Y. E., 2023, "Monolithically-Stacked Thin-Film Solid-State Batteries," Commun. Chem., **6**(1), p. 110.

[34] Waldmann, T., Bisle, G., Hogg, B.-I., Stumpp, S., Danzer, M. A., Kasper, M., Axmann, P., and Wohlfahrt-Mehrens, M., 2015, "Influence of Cell Design on Temperatures and Temperature Gradients in Lithium-Ion Cells: An In Operando Study," J. Electrochem. Soc., **162**(6), pp. A921–A927.

[35] Han, X., Ouyang, M., Lu, L., Li, J., Zheng, Y., and Li, Z., 2014, "A Comparative Study of Commercial Lithium Ion Battery Cycle Life in Electrical Vehicle: Aging Mechanism Identification," J. Power Sources, **251**, pp. 38–54.

[36] Fly, A., and Chen, R., 2020, "Rate Dependency of Incremental Capacity Analysis (dQ/dV) as a Diagnostic Tool for Lithium-Ion Batteries," J. Energy Storage, **29**, p. 101329.

[37] Kurzweil, P., Scheuerpflug, W., Frenzel, B., Schell, C., and Schottenbauer, J., 2022, "Differential Capacity as a Tool for SOC and SOH Estimation of Lithium Ion Batteries Using Charge/Discharge Curves, Cyclic Voltammetry, Impedance Spectroscopy, and Heat Events: A Tutorial," Energies (Basel), **15**(13), p. 4520.

[38] Flores, E., Novák, P., Aschauer, U., and Berg, E. J., 2020, "Cation Ordering and Redox Chemistry of Layered Ni-Rich Li xNi1-2 yCo yMn yO2: An Operando Raman Spectroscopy Study," Chem. Mater., **32**(1), pp. 186–194.

[39] Orangi, S., Manjong, N., Clos, D. P., Usai, L., Burheim, O. S., and Strømman, A. H., 2024, "Historical and Prospective Lithium-Ion Battery Cost Trajectories From a Bottom-Up Production Modeling Perspective," J. Energy Storage, **76**, p. 109800.